(Received 3 February 2026, Accepted 16 March 2026, Scheduled 21 April 2026)

High Isolation UWB MIMO Notch Antenna Based on Metamaterials

Xuemei Zheng[1,*], Yunan Zhang[2], and Linfei Yue[2]

[1]*Key Laboratory of Modern Power System Simulation and Control and Renewable Energy Technology Ministry of Education, Northeast Electric Power University, Jilin, China*
[2]*Northeast Electric Power University, Jilin, China*

ABSTRACT: This paper proposes a compact UWB MIMO antenna with band-notched characteristics and high isolation. With a miniaturized footprint of 60×32 mm, the antenna covers the full UWB spectrum of 3.1–13 GHz. A core structural innovation lies in the design of a novel SRR metamaterial unit, which exhibits superior high-frequency decoupling capability by regulating electromagnetic wave propagation; combined with the synergistic decoupling mechanism of a meandered-line radiating patch and an I-shaped DGS for low-frequency isolation enhancement, the antenna achieves an excellent measured isolation (S_{21}) of better than -21 dB across the entire operating band. Additionally, four precise notched bands (3.3–3.4 GHz WiMAX, 4.4–5.0 GHz n79, 5.15–5.825 GHz WLAN, 7.9–8.4 GHz) are realized via strategically etched slots on radiating elements to suppress interference. Verified by measurements, the measured ECC is as low as below 0.018, and the diversity gain maintains stability near the ideal 10 dBi. The antenna exhibits stable radiation patterns throughout the impedance bandwidth, accompanied by outstanding diversity performance.

1. INTRODUCTION

Although essential for enhancing the capacity and efficiency of 5G and IoT systems [1], designing multiple-input multiple-output (MIMO) antennas for UWB applications is challenging, as they must achieve high inter-element isolation and effective band-notching while maintaining a compact form factor, which is difficult with traditional methods.

Metamaterials, leveraging unique electromagnetic properties, such as negative refractive index [2], zero refractive index, and reconfigurability, offer significant potential for enhancing antenna performance. Among them, split-ring resonators (SRRs) have been widely adopted to improve isolation between antenna elements. Their distinctive ability to manipulate electromagnetic waves at subwavelength scales sets them apart from conventional methods like parasitic elements or decoupling networks. By exciting localized resonant modes [3], SRR can suppress mutual coupling without compromising bandwidth or miniaturization. Furthermore, their reconfigurability and capability to exhibit negative permeability enable the precise tuning of isolation across ultra-wideband spectra, making SRRs a more efficient and flexible solution than traditional techniques.

For instance, Su et al. incorporated Koch fractal decoupling branches and a hexagonal dual-SRR array to develop a four-port ultra-wideband (UWB) MIMO antenna, achieving over 20 dB of isolation across most of the operating band [4]. Gao et al. integrated a complementary split-ring resonator (CSRR) into the ground plane to design a compact triple-notched UWB MIMO antenna, effectively improving both isolation and broadband performance [5]. Mishra et al. employed an SRR-based partition between antenna elements to significantly enhance isolation in a compact cylindrical dielectric resonator antenna [6]. This work presents a compact UWB-MIMO antenna design that features a synergistic decoupling approach. Compared with existing solutions, directly embedding split-ring resonators (SRRs) into the antenna radiator significantly saves space while maintaining structural integrity. The proposed structure achieves port isolation exceeding -21 dB across the 3.1–13 GHz band without requiring additional decoupling components. This integrated configuration not only improves isolation efficiency but also maintains a compact form factor, offering significant advantages over conventional external decoupling methods.

2. ANTENNA DESIGN

2.1. Design of UWB-MIMO Antennas

This paper presents an innovative miniaturized ultra-wideband antenna design. The final dimensions of the antenna are 60 mm × 32 mm × 1.6 mm, as shown in Figure 1. The antenna utilizes FR-4 as the dielectric substrate material, with a permittivity (dielectric constant) of 4.4 and a loss tangent ($\tan\delta$) of 0.02. The front structure of the antenna consists of two radiating patches, which are fed by microstrip lines. The distance between the two radiation patch antennas is 24.4 mm. The overall antenna structure includes a dielectric substrate, fan-shaped radiating patches, meander-line structure patches, metamaterial structures with split-ring resonators, and a bottom I-shaped defected ground structure. The microstrip antenna model utilizes the electromagnetic software High Frequency Structure Simulator (HFSS) to optimize and simulate the design of the UWB MIMO antennas based on metamaterials. The antenna layout is illustrated in Figure 1, with optimized dimensions summarized in Table 1.

* Corresponding author: Xuemei Zheng (zhengxuemei@neepu.edu.cn).

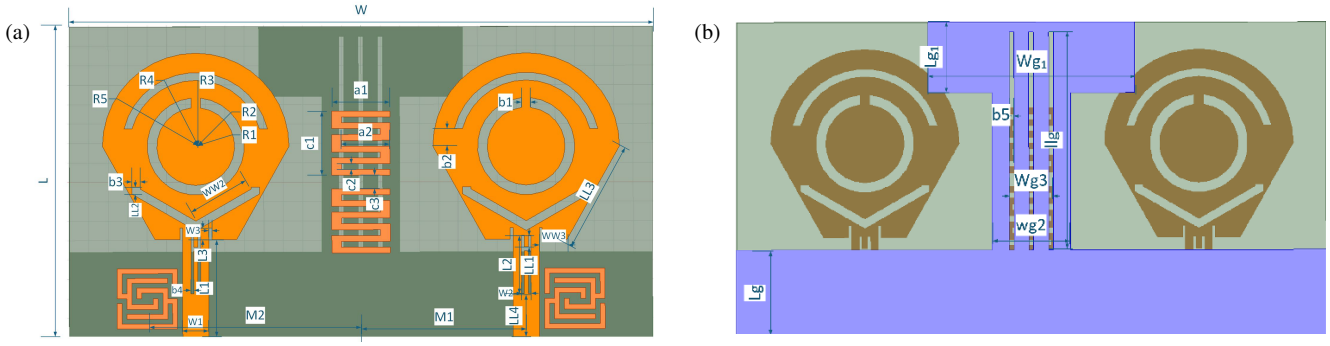

FIGURE 1. Antenna: (a) Front view; (b) Back view.

TABLE 1. Dimensions of the optimized antenna structure (Unit: mm).

Parameter	W	L	W_1	L_1	L_2	W_2	L_3	W_3	LL_1	LL_2	WW_2	R_1
Unit (mm)	60	32	2.7	10.2	6	1	1.2	0.3	1.2	0.7	6.6	4
Parameter	R_2	R_3	R_4	R_5	M_2	WW_3	L_5	Lg	Lg_1	Wg_1	Wg_2	Wg_3
Unit (mm)	5	6.8	7.6	9.6	22	2.8	11	8.8	7.2	21	8	4.5
Parameter	llg	b_1	b_2	b_3	b_4	b_5	a_1	a_2	c_1	c_2	c_3	LL_3
Unit (mm)	23.2	0.9	2.2	0.8	0.3	0.5	6	5	6.6	0.6	1.4	11

To enhance antenna performance, a slotting technique was applied to the circular patch (Figure 2(a)), improving the electric field distribution and broadening the operating bandwidth. Additionally, an I-shaped ground plane structure (Figures 2(b)–2(c)) was introduced to enhance isolation by optimizing current paths. This structural design enhances the antenna isolation by optimizing the current path, thereby effectively reducing mutual interference during signal transmission and ensuring the stability and reliability of the signals. After these optimizations, the antenna achieved an ultra-wideband operating frequency range of 3.1–13 GHz, covering several important communication bands and demonstrating excellent wideband performance. Furthermore, the antenna exhibits poor isolation performance, which fails to meet the stringent requirements of modern communication systems for high-performance antennas.

2.2. Notched Structure Design

In practical communication applications, interference signals often severely disrupt the normal operation of communication frequency bands, making notching capability an essential feature for UWB antenna design. Currently, two common methods for achieving notching in UWB antennas are the slot-line method and the addition of stubs. In this paper, we choose the slot-line method to implement the notching characteristics of the antenna. The slot-line method has minimal impact on the original antenna structure and allows for precise control over specific frequency bands. It can effectively suppress specific interference bands and ensure the stability and reliability of the communication system.

Etching slots of different shapes and lengths on the antenna patch can generate notch characteristics. These slots act as quarter-wavelength resonators that modify the surface current distribution on [7]. The first step in implementing this notch is to determine the dimensions of the slot structure. The theoretical length L of the slot, which corresponds to the center frequency of the notch band [8], is given by the formula:

$$L = \frac{c}{f_{notch}\sqrt{2(\varepsilon_r + 1)}} \tag{1}$$

Here, f_{notch} represents the center frequency of the notch; c represents the speed of light; and ε_r represents the relative permittivity of the dielectric substrate. The total lengths L_1, L_2, L_3, and L_4 of the C-shaped slot, semi-circular slot, V-shaped slot, and H-shaped slot can be calculated using Equation (1).

This paper presents a UWB MIMO antenna notching design based on a multi-slot-line structure. Controlling the structural parameters of different shaped slot lines effectively suppresses interference signals in multiple communication bands. Specifically, three different slot-line structures are designed on the fan-shaped radiating patch: a circular slot for 3.3–3.4 GHz WiMAX band, a semi-circular slot for 4.4–5.0 GHz n79 band, and a V-shaped slot for 5.15–5.85 GHz WLAN band. Additionally, an H-shaped slot is introduced in the feed line to achieve notching in the 7.9–8.4 GHz uplink satellite band. The sizes of all notching structures are precisely calculated based on the center frequencies of the target bands and optimized for the best performance.

2.3. Parametric Study

A parametric study of the ground plane was conducted to optimize the antenna's impedance matching and radiation performance. As shown in Figure 3, for the I-shaped Defected Ground Structure (DGS), increasing slot length (Lg) from 6.8 mm to 10.8 mm shifts low-frequency isolation improvement downward, with $Lg = 8.8$ mm yielding optimal performance at

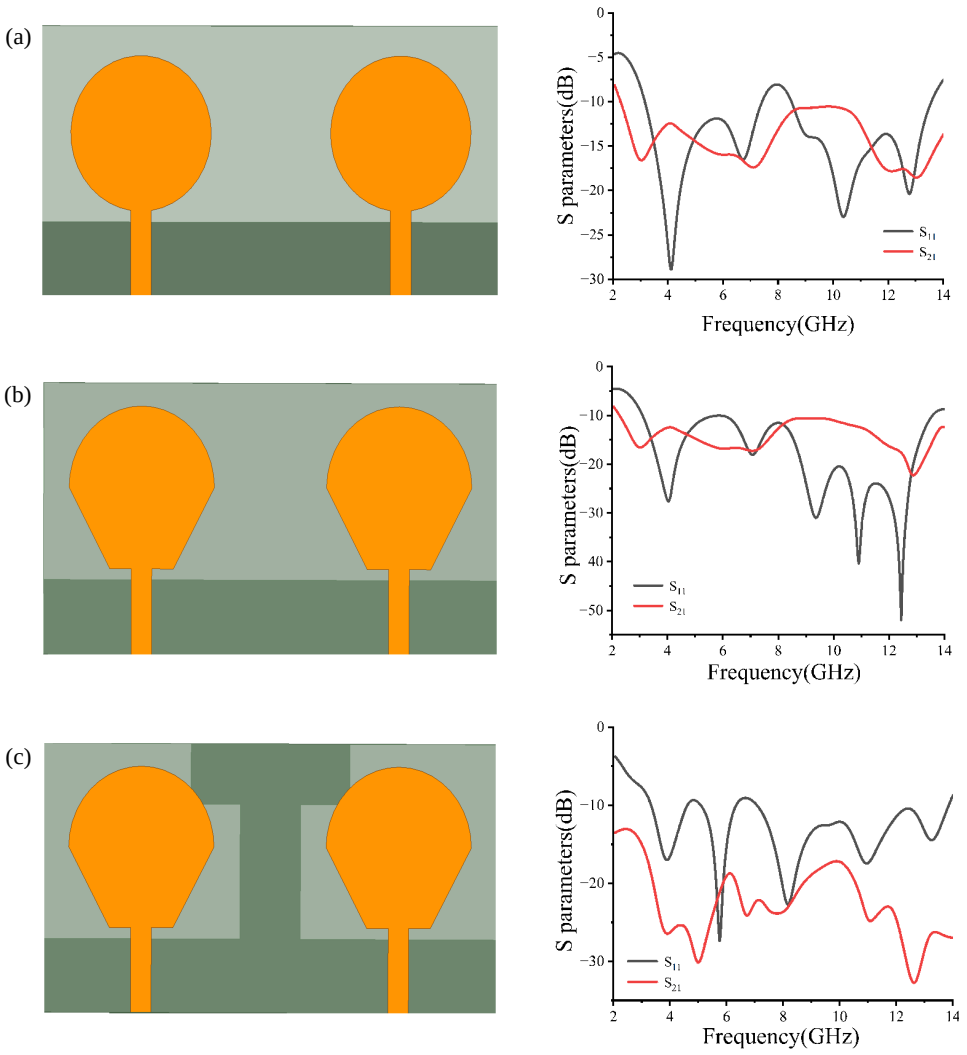

FIGURE 2. MIMO antenna design steps and S parameters: (a) Initial MIMO antenna; (b) Changes in the cutting angle; (c) Ground plane changes.

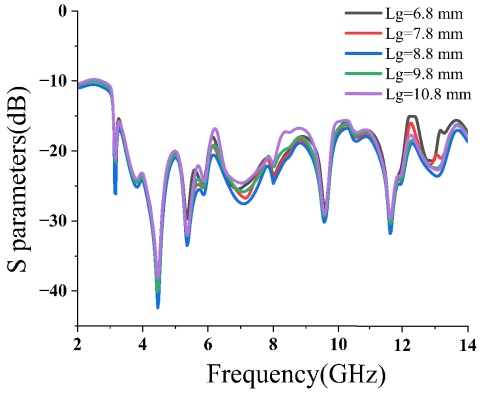

FIGURE 3. Simulated S_{21}-parameter responses of the MIMO antenna system with varying (Lg).

~4.5 GHz. The DGS width ($Wg_1 = 21$ mm) controls isolation improvement magnitude. The bridge width ($Wg_3 = 4.5$ mm) affects decoupling bandwidth. For the feedline, the width of 1 mm achieves 50 Ω impedance matching. A ±0.2 mm feedline width variation causes less than 1 dB return loss degradation, confirming manufacturing robustness.

2.4. Decoupling Design of MIMO Antenna

In the ultra-wideband antenna, the introduction of a notched structure may enhance the coupling effect between antenna elements and reduce the isolation degree due to the change of the surface current distribution, which will affect the performance of the UWB-MIMO antenna. As shown in Figure 4, to improve the isolation degree, linear slots are etched on the back of the dielectric substrate to enhance the electromagnetic interference effect and reduce energy leakage and interference. Meanwhile, a meandered patch is introduced on the front of the substrate. This structure changes the propagation path of the electromagnetic wave, optimizes the radiation characteristics, and suppresses the crosstalk between antennas.

Figure 5 shows the S-parameter comparison diagram, through the synergistic effect of these two structures. The S_{21} parameter has basically reached below −20 dB in the low-frequency and mid-frequency bands, and the isolation between antennas is significantly enhanced. This not only effectively reduces signal interference between antennas but also improves the overall performance and reliability of the system, providing a strong guarantee for the efficient appli-

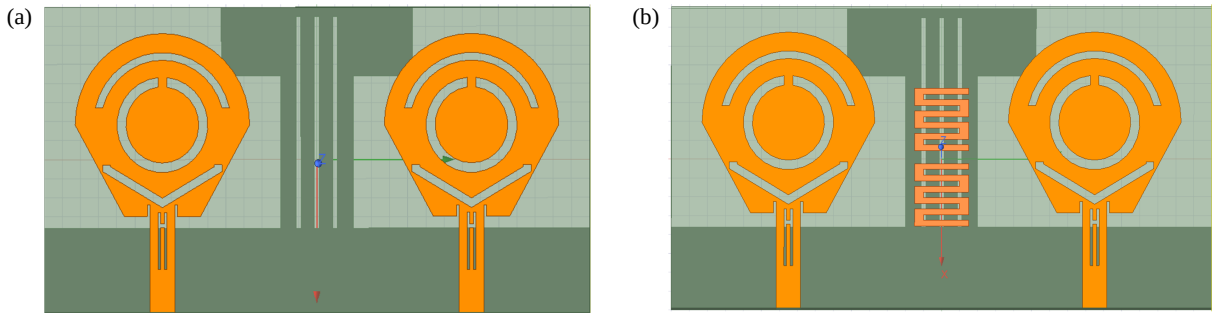

FIGURE 4. MIMO antenna: (a) Without curved structure; (b) With a curved structure.

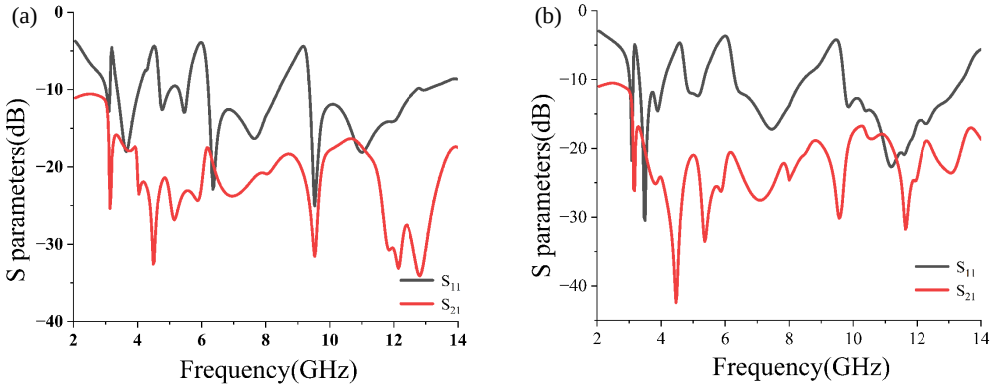

FIGURE 5. S-parameter comparison diagram: (a) Without curved structure; (b) With curved structure.

cation of UWB-MIMO antennas in complex communication environments.

3. METAMATERIAL UNIT DESIGN AND ANALYSIS

3.1. Metamaterial Cell Design

In this section, a centrally symmetric split-ring structured metamaterial unit cell is designed. The outer side length of the innermost ring is 6.2 mm; the line width is 0.5 mm; and the gap between the square rings is 0.5 mm. The outermost ring has an opening of 0.5 mm and is connected to the second layer ring. The opening of the second-layer ring is horizontally connected to the bottom line of the innermost ring. The dielectric substrate is a 12 mm $\times$ 12 mm square FR4 board with a thickness of 1.6 mm, a dielectric constant of 4.4, and a loss tangent angle $\tan\sigma$ of 0.02.

The designed metamaterial unit cell incorporates a double-spiral configuration, as illustrated in Figure 6(b). The equivalent circuit model is established based on the lumped-element equivalence principle applied to electromagnetic structures. Within this model, the series inductance L_s arises from the current path inductance along the metallic trace of the metamaterial, which is governed by its physical length and width. The parallel inductance L_d and capacitance C_d collectively form an LC resonant circuit, corresponding to the closed or resonant portion of the structure. Specifically, L_d is determined by the geometric parameters of the ring, while C_d is influenced by the spacing of structural gaps. The grounding capacitance C_g represents the capacitive coupling between the metamaterial structure and the ground plane, which depends on the permittivity and thickness of the substrate. The equivalent inductance and capacitance of the double-spiral structure are expressed as follows:

$$C_x = \frac{\omega_c}{2Z_0(\omega_0^2 - \omega_c^2)} \tag{2}$$

$$L_x = \frac{1}{4\pi^2 f_0^2 C_x} \tag{3}$$

The ω_0 denotes the resonant angular frequency of the parallel resonant circuit, and ω_c represents the cutoff angular frequency.

To quantify the equivalent circuit model, the component values are derived from physical dimensions. For the SRR with a total spiral trace length of $\sim$35 mm and width of 0.5 mm, the series inductance $L_s \approx 8.2$ nH. The parallel inductance $L_d \approx 3.5$ nH is determined by the innermost ring geometry, while the gap capacitance $C_d \approx 0.07$ pF is governed by the 0.5 mm gap width and substrate permittivity ($\varepsilon_r = 4.4$). The grounding capacitance $C_g \approx 0.15$ pF represents coupling through the 1.6 mm FR4 substrate. Substituting $L_d \approx 3.5$ nH and $C_d \approx 0.07$ pF into $f_0 = 1/(2\pi\sqrt{(L_d \cdot C_d)})$ yields $\sim$10.2 GHz, closely matching the simulated $\sim$10 GHz in Figure 6(a), validating the model. The SRR loading introduces less than 5 Ω perturbation to the antenna input impedance, maintaining $S_{11} < -10$ dB across the operating band.

This equivalent circuit model establishes a closed-form mapping from physical dimensions to electromagnetic response, enabling a theory-guided design approach: the target decoupling

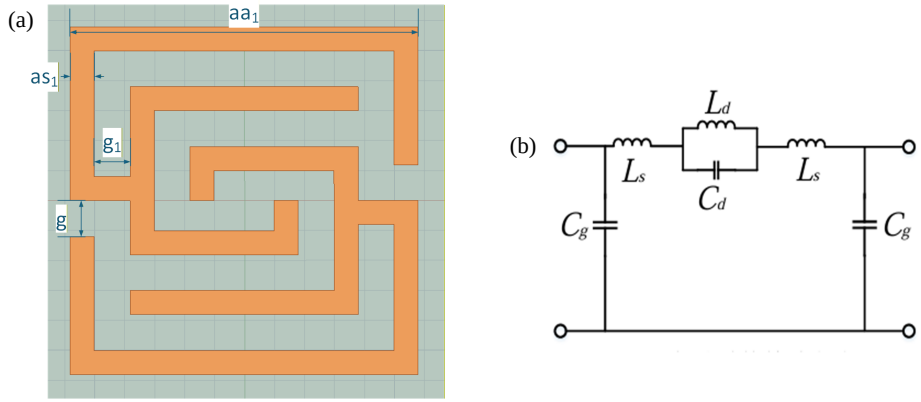

FIGURE 6. (a) Metamaterial unit structure diagram; (b) Equivalent circuit diagram.

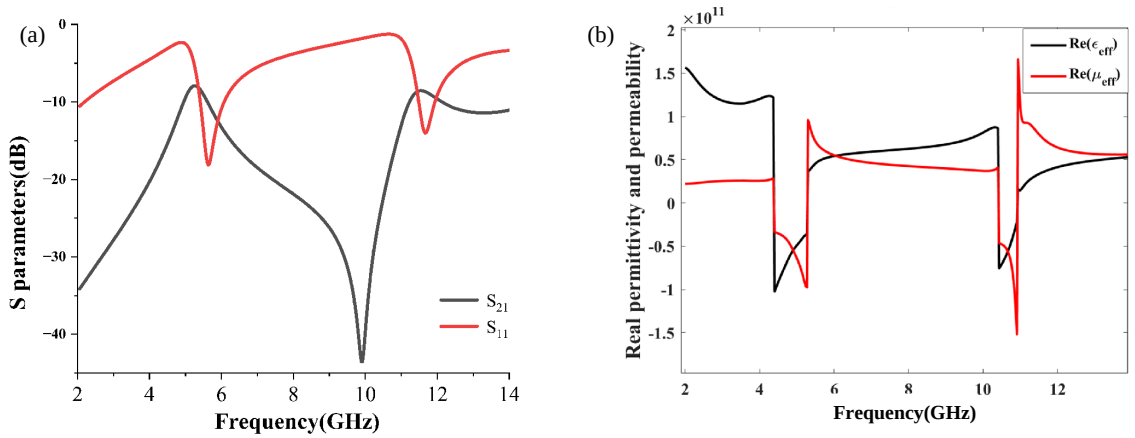

FIGURE 7. (a) Plot of the S-parameter structure; (b) Plot of the extracted equivalent parameter values.

frequency f_0 is determined from isolation requirements, and the required $L_d \cdot C_d$ product is calculated accordingly, where L_d is controlled by the inner ring geometry and C_d by the gap width g independently — a key advantage of the proposed double-spiral topology. The model reliability is validated through a three-level verification: the circuit predicts $f_0 \approx 10.2$ GHz. HFSS simulation confirms resonance at ∼10 GHz ($< 2\%$ deviation, Figure 7(a)), and the fabricated prototype measurements verify the corresponding isolation improvement in the 8–12 GHz band (Figure 16). Furthermore, the parametric sweep of g (Section 3.2) confirms the circuit-predicted monotonic relationship $f_0 \propto \sqrt{g}$: increasing g from 0.3 to 0.7 mm shifts the resonance from 9.2 to 10.8 GHz, in quantitative agreement with the model. The SRR presents a high resonant impedance $\sqrt{(L_d/C_d)} \approx 224\,\Omega$, far exceeding the $50\,\Omega$ system impedance, which ensures effective decoupling without loading the feed network — thus preserving broadband impedance matching across the entire 3.1–13 GHz band.

The metamaterial model is established in HFSS. The designed metamaterial unit cell is surrounded by an air box. Two wave ports are placed on the left and right sides of the air box, and appropriate boundary conditions (i.e., perfect magnetic conductor (PMC) and perfect electric conductor (PEC)) are set on the top and bottom surfaces and the front and back surfaces of the air box, respectively.

3.2. Simulation Analysis

The S_{11} and S_{21} parameters of the designed metamaterial cell were obtained using HFSS simulation, as shown in Figure 7.

Figure 7(a) presents the S-parameters of the metamaterial unit cell. From the figure, it can be observed that the metamaterial unit cell resonates near 10 GHz. The transmission parameters of the metamaterial unit cell are input into the Matlab program of the S-parameter inversion algorithm, and the equivalent electromagnetic parameters of the metamaterial unit cell are obtained through calculation. The solution process of the S-parameter inversion algorithm is as follows:

$$S_{11} = \frac{Z}{Z_0 + Z} + \frac{Z_0}{Z} \mathrm{e}^{-2\mathrm{i}\delta} \tag{4}$$

$$S_{21} = \frac{2Z_0 Z}{Z_0 + Z} \mathrm{e}^{-\mathrm{i}\delta} \tag{5}$$

Here, $\delta = 2\pi nd/\lambda$, Z_0 is the impedance of free space, and λ is the wavelength.

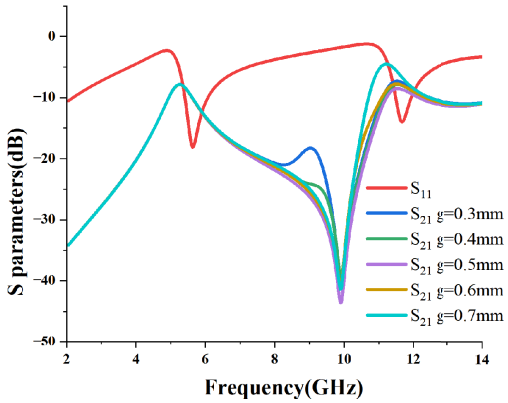

FIGURE 8. Simulated S_{21}-parameter responses of the MIMO antenna system with varying SRR gap width (g).

The equivalent refractive index n and relative impedance Z are solved as shown in (6) and (7):

$$z = \sqrt{\frac{(1+S_{11})^2 + S_{21}^2}{(1-S_{11})^2 - S_{21}^2}} \tag{6}$$

$$n = \frac{\arccos\left(\frac{(1-S_{11})^2+S_{21}^2}{2S_{21}}\right)}{kd} \tag{7}$$

Here, $k = 2\pi f/c$, f is the frequency, and c is the speed of light.

The equivalent dielectric constant and permeability of metamaterials are solved as shown in (8) and (9):

$$\varepsilon_e = n^2 \tag{8}$$

$$\mu_e = \left(\frac{Z}{Z_0}\right)^2 \tag{9}$$

From Figure 7(b), it can be seen that the proposed unit cell meets the metamaterial design requirements of this chapter in terms of electromagnetic characteristics of equivalent permittivity and equivalent permeability.

To evaluate design robustness, a parametric study of the SRR gap width (g) was conducted by sweeping g from 0.3 mm to 0.7 mm. Figure 8 depicts the simulated S_{21}-parameter responses. The key findings are: (1) the SRR resonant frequency shifts upward from 9.2 GHz to 10.8 GHz with increasing gap width, consistent with reduced gap capacitance in the equivalent circuit model; (2) maximum isolation improvement of approximately 8 dB at 10 GHz is achieved at the optimal value $g = 0.5$ mm; (3) isolation performance remains better than -19 dB for ± 0.1 mm gap width variations, demonstrating robustness to typical printed circuit board (PCB) manufacturing tolerances; (4) the effective decoupling bandwidth of approximately 4 GHz (8–12 GHz) remains stable across all tested gap widths.

4. OVERALL MIMO ANTENNA STRUCTURE DESIGN PROCESS

To mitigate the electromagnetic coupling between antenna elements, the metamaterial unit cells proposed in the previous section are incorporated into the UWB notched antenna structure, as shown in Figure 9. The metamaterials are symmetrically arranged on both sides of the feedline on the dielectric substrate.

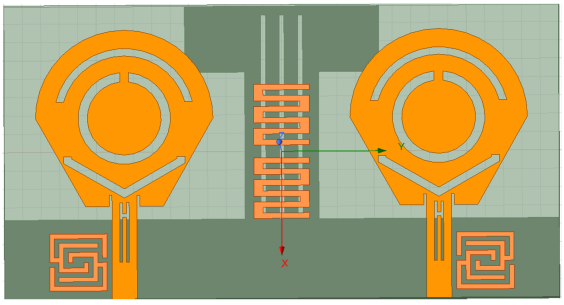

FIGURE 9. Structural diagram of the MIMO antenna.

4.1. S-Parameter Simulation Analysis

As shown in Figure 10, the S-parameters of MIMO antennas in two different cases, with and without metamaterials, are presented. Figures 10(a) and (b) correspond to the S_{11} and S_{21} parameters of the antennas in the cases without metamaterials and with metamaterials, respectively. It can be seen from the figure that the incorporation of metamaterials significantly improves isolation ($S_{21} < -21$ dB) without compromising low-frequency performance. It effectively reduces the electromagnetic coupling between the two antenna elements in the high-frequency band. At the same time, it significantly improves the impedance matching of the antenna array near 5 GHz and 7 GHz. These improvements enable the optimized MIMO antenna array to have a much wider bandwidth, covering the broad range of 3.1 GHz to 13 GHz. Moreover, the specific value of S_{21} is less than -21 dB, indicating a significant reduction in electromagnetic mutual coupling. The performance of the antenna array has been significantly enhanced in multiple aspects, providing strong support for the efficient and stable operation of related communication systems.

The physical mechanism behind the high-frequency isolation improvement is attributed to the SRR's negative effective permeability (μ-negative) near its $\sim$10 GHz resonance, which creates an electromagnetic bandgap that blocks surface wave propagation — the dominant high-frequency coupling mechanism. The SRR excites localized resonant currents that absorb coupling energy and destructively interfere with propagating surface waves, effectively terminating the inter-element coupling path. This targeted high-frequency decoupling complements the low-frequency isolation provided by the meandered-line patch and I-shaped DGS, achieving synergistic broadband isolation across the entire 3.1–13 GHz band.

4.2. Surface Current Distribution Analysis

Figure 11 illustrates the surface current density distribution of the MIMO antenna with and without metamaterials. Darker colors indicate higher current density, while lighter colors indicate lower current density. The left figure is without metamaterials, and the right one is with metamaterials. It can be seen that after placing the metamaterials symmetrically on the sides of the two antenna feed lines, the surface current density

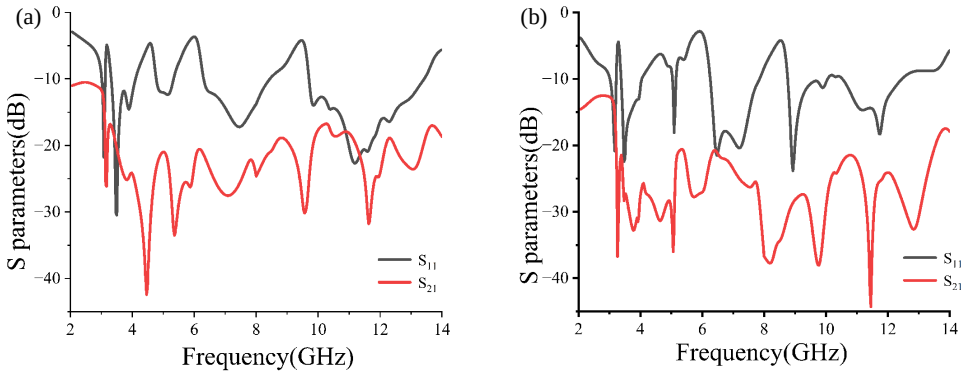

FIGURE 10. S-parameter comparison diagram: (a) Without metamaterial unit; (b) With metamaterial unit.

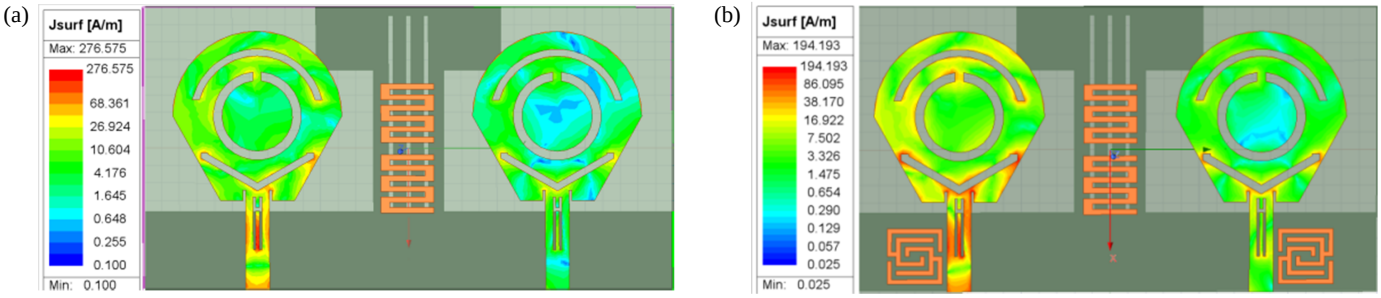

FIGURE 11. Surface current distribution of the MIMO antenna: (a) Without metamaterials, (b) With metamaterials.

on the left antenna element becomes significantly higher. The designed metamaterials can effectively reduce the electromagnetic coupling between adjacent elements.

4.3. Antenna Radiation Pattern

Figure 12 illustrates the radiation patterns of the antenna at different frequency bands. The patterns exhibit well-defined main lobes and good symmetry across the operating band. It can be observed that as the frequency increases, the beamwidths of both the H-plane and E-plane radiation patterns become noticeably narrower, indicating a more concentrated radiation energy and a significant enhancement in antenna directivity. This behavior reflects the increase in the electrical size (relative to the wavelength) of the microstrip antenna at higher frequencies, which leads to a more focused radiation pattern and narrower beamwidth. Such a characteristic enables the antenna to better adapt to varying communication requirements across different frequency bands, making it suitable for applications such as long-range directional transmission.

In addition, the radiation patterns are analyzed in terms of co-polarization and cross-polarization characteristics. At all representative frequencies, the co-polarized component remains dominant in both the E-plane and H-plane, forming the principal radiation beam with good pattern stability and symmetry. By contrast, the cross-polarized component is significantly lower than the co-polarized one over the main radiation direction, which indicates good polarization purity and limited undesired orthogonal field radiation. As the frequency increases, the co-polarized main beam becomes slightly narrower, while the cross-polarization level remains under acceptable control without introducing severe pattern distortion.

4.4. Gain and Efficiency

Figure 13 presents the peak gain and radiation efficiency of the proposed ultra-wideband antenna across the operating frequency band. The antenna exhibits a gain ranging from -0.8 dBi to 6.2 dBi within the 3.1–13 GHz frequency range. The radiation efficiency remains at a high level throughout most of the band, indicating effective energy radiation performance.

Distinct notch characteristics are clearly observable in both the gain and efficiency curves within the designated notched bands. These notched features confirm effective interference suppression in the target frequency ranges. Outside these bands, the antenna maintains stable performance with gain generally exceeding 3.5 dBi and radiation efficiency typically remaining above 80%, demonstrating its suitability for ultra-wideband applications.

4.5. Diversity Characteristics of the MIMO Antenna

The Envelope Correlation Coefficient (ECC) serves as a key indicator for assessing the diversity performance and channel independence of MIMO systems. A lower ECC value signifies improved antenna independence and diversity gain. The ECC

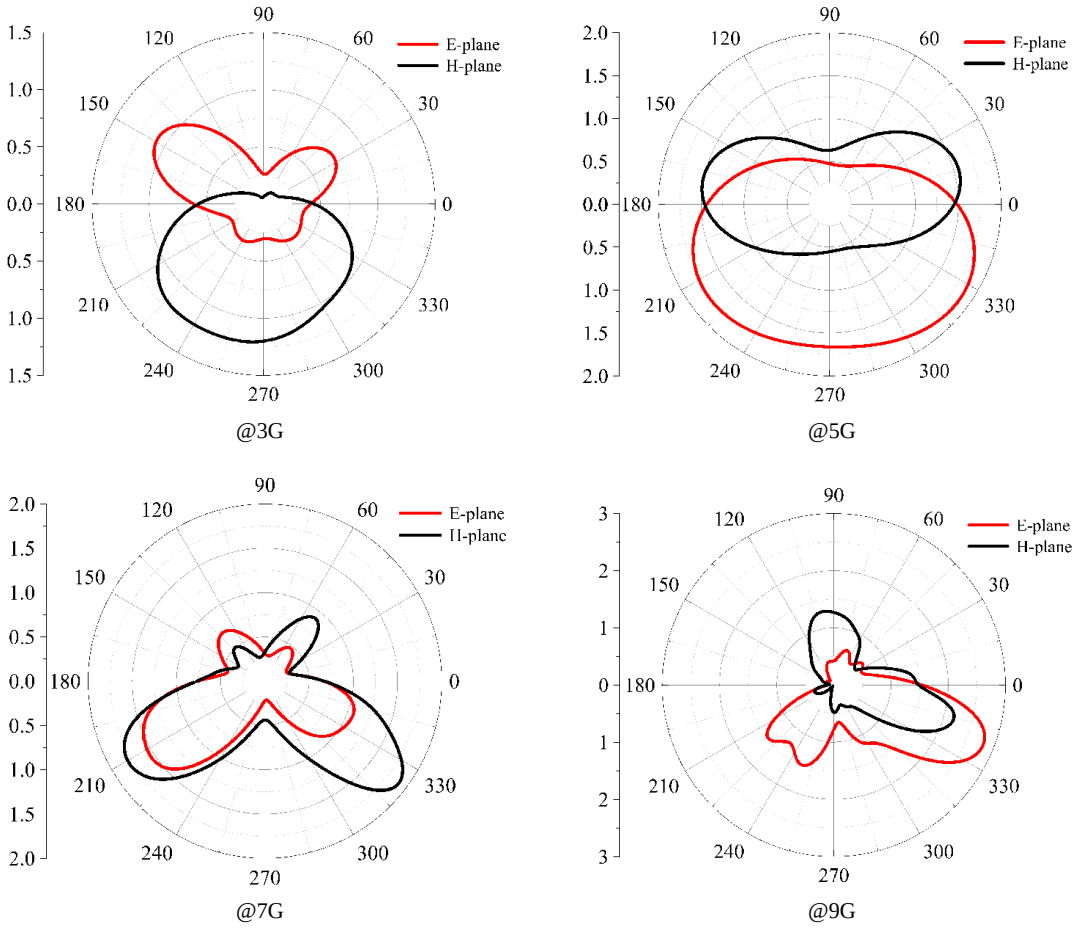

FIGURE 12. Radiation direction of the antenna.

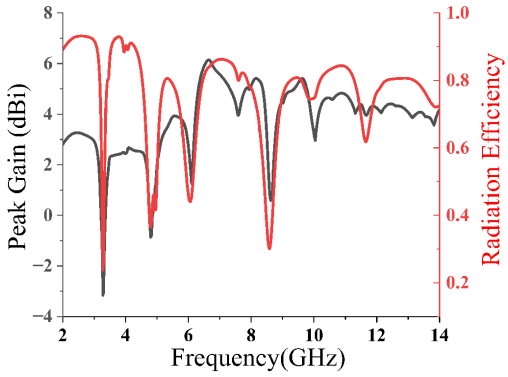

FIGURE 13. Gain and efficiency of the proposed antenna.

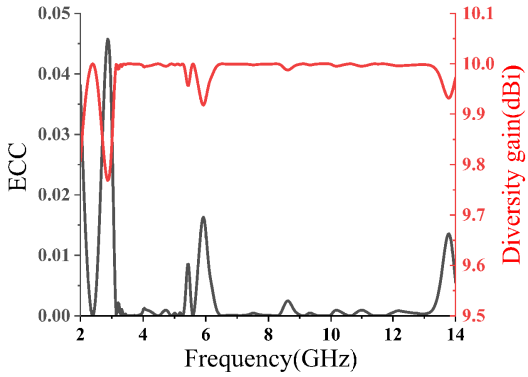

FIGURE 14. ECC and diversity gain of the proposed antenna.

can be obtained from the following expression:

$$\rho_e = \frac{\left|S_{11}^* S_{12} + S_{21}^* S_{22}\right|^2}{\left(1-\left|S_{11}\right|^2-\left|S_{21}\right|^2\right)\left(1-\left|S_{22}\right|^2-\left|S_{12}\right|^2\right)\eta_1\eta_2} \quad (10)$$

Diversity gain (DG) quantifies the signal-to-noise ratio improvement achieved by MIMO systems in fading environments. Calculated from the envelope correlation coefficient, DG characterizes the system's capability to mitigate multipath fading and enhance link reliability. A higher DG value corresponds to improved diversity performance. The expression for DG is given by:

$$\mathrm{DG} = \sqrt{1-(\mathrm{ECC})^2} \quad (11)$$

Figure 14 depicts the simulated ECC and DG plots of the proposed MIMO antenna. Across the 3–13 GHz operating band, the ECC remains below 0.018, demonstrating excellent diversity performance. while the diversity gain remains stable near the ideal value of 10 dBi. A clear inverse relationship is observed between the two parameters, and slight degradations in diversity gain correspond to minor peaks in ECC. These results

TABLE 2. Comparison of MIMO antenna array measurement results among the studies.

Reference	Notched band	Size (mm^2)	Isolation (dB)	ECC	Frequency band (GHz)	Gain (dBi)	Radiation efficiency
[9]	4	$45 * 45$	-17	0.02	3.1–13.1	4	73%
[10]	4	$40 * 40$	-17	0.03	2.9–14	5	75%
[11]	4	$70 * 41$	-17	0.012	3.1–12	5.3	-
[12]	4	$45 * 45$	-16	0.02	3.1–11	3.6	-
[13]	3	$24 * 20$	-	-	3.1–12	3.7	-
[14]	4	$39 * 39$	-22	0.02	3.1–13.7	4.6	-
[15]	7	35×34	-	-	2.4–13.1	4.14	-
[16]	6	44×39	-	-	3.3–15.9	4.14	68–88%
[17]	3	30×44	-	-	2.38–5.81	2.06	82.9%
This paper	4	$60 * 32$	-21	0.018	3.1–13	6.2	80%

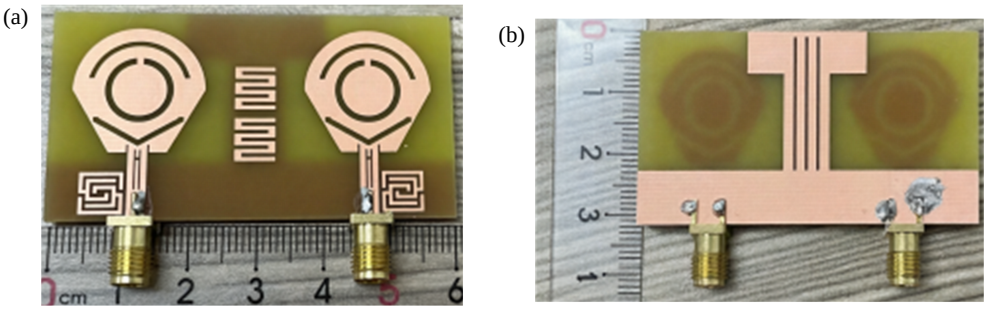

FIGURE 15. Physical processing diagram: (a) Front view; (b) Back view.

validate the effective diversity performance of the proposed antenna, demonstrating robust MIMO operation over the ultra-wideband spectrum.

The superior gain of 6.2 dBi is attributed to three synergistic factors: (i) the optimized fan-shaped patch geometry maximizing effective radiation aperture; (ii) SRR suppression of mutual coupling preserving independent element radiation efficiency; (iii) complete ground plane design minimizing back-lobe radiation loss. Regarding the size trade-off, while the $60 \times 32\,mm^2$ footprint is larger than some referenced designs, it accommodates four notch bands and integrated SRR metamaterial — features absent in more compact designs. When normalized by functional density (features per unit area), the proposed design is highly competitive. The dominant improvement parameter is the SRR metamaterial, contributing 5–8 dB of high-frequency isolation enhancement and directly reducing ECC from approximately 0.05 (without SRR) to below 0.018.

4.6. Comparative Analysis of Antenna Array Elements

The proposed antenna, while featuring a larger physical dimension of $60 * 32\,mm^2$ compared to most referenced designs, exhibits notable advantages in terms of overall performance and functional integration. As summarized in Table 2, the antenna achieves a peak gain of 6.2 dBi and a radiation efficiency of 80%, exceeding the radiative performance of most comparable

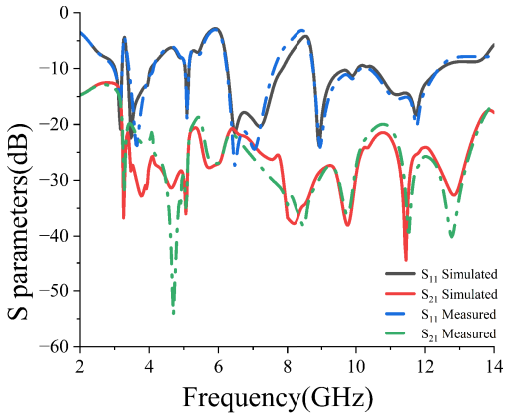

FIGURE 16. Measured and simulated S-parameters of the designed MIMO antenna.

structures. It also demonstrates a high port isolation of -21 dB and a low envelope correlation coefficient of 0.018, indicating strong diversity performance. Furthermore, the design incorporates four notch bands across an ultra-wide operating bandwidth from 3.1 to 13 GHz, providing effective multi-band interference rejection without degrading gain or efficiency.

Table 2 compares the proposed antenna with representative UWB MIMO designs. The performance advantages are analyzed from the SRR equivalent circuit model. (a) The high gain of 6.2 dBi originates from the reactive decoupling nature of the

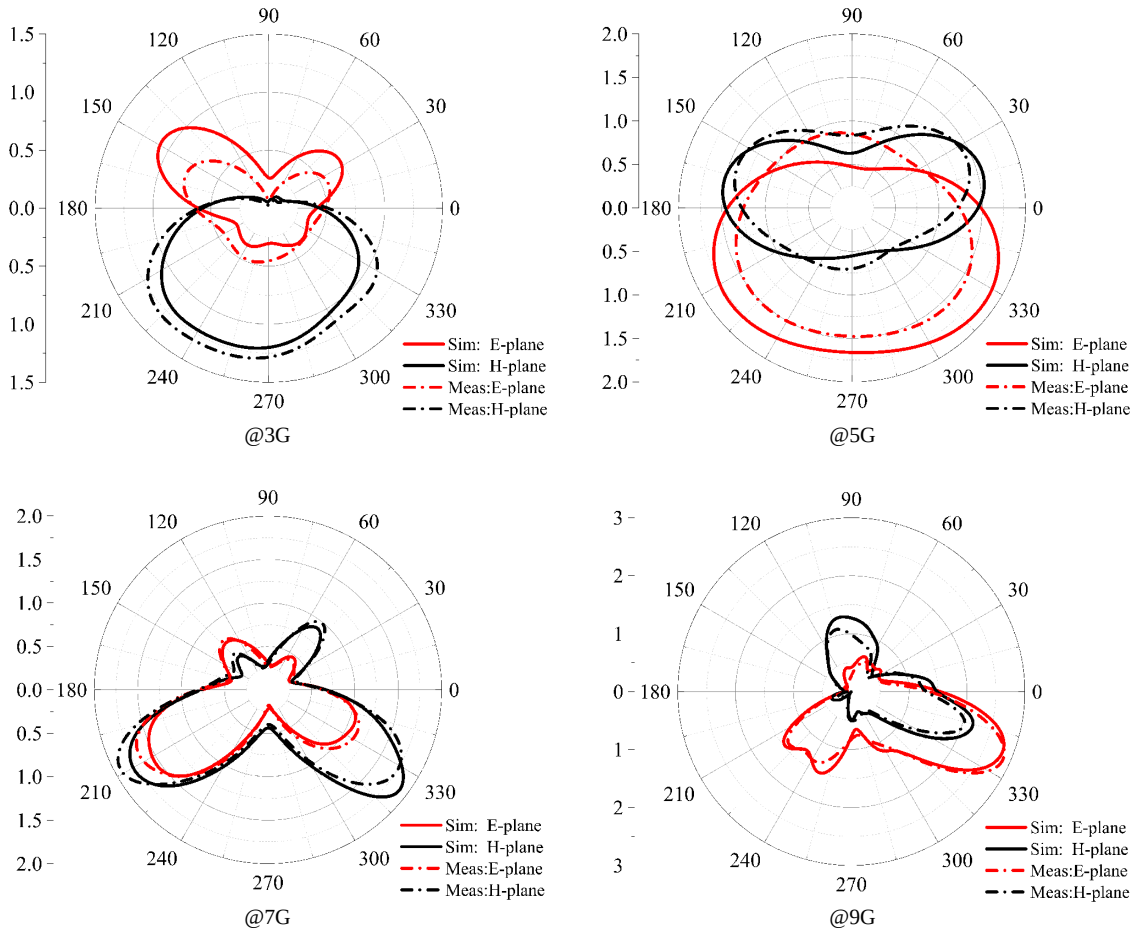

FIGURE 17. Measured and simulated radiation patterns.

SRR. In the lumped-element model, the parallel L_d-C_d tank ($L_d \approx 3.5$ nH, $C_d \approx 0.07$ pF) presents a resonant impedance $Z_0 = \sqrt{(L_d/C_d)} \approx 224\,\Omega$, approximately 4.5 times the 50 Ω system impedance. This high impedance ratio ensures that coupling energy is absorbed through localized LC resonance and reradiated, rather than dissipated resistively in the feed network. The reactive trap preserves total radiated power and maintains 80% radiation efficiency, unlike resistive decoupling methods that inherently introduce ohmic loss and reduce gain. (b) The $60 \times 32\,\text{mm}^2$ footprint results from multi-function integration enabled by the L_d-C_d independent tunability: L_d is controlled by the inner ring geometry and C_d by the gap width g, two physically orthogonal parameters. This allows the SRR to be embedded as a single unit cell, avoiding the spatial overhead of periodic structures, such as EBG arrays. The area accommodates six coexisting functional structures (four notch-band slots, SRR, and I-shaped DGS), achieving higher functional density than smaller designs with fewer functions. (c) The circuit model identifies g as the dominant parameter, directly governing C_d and thus $f = 1/(2\pi\sqrt{(L_d \cdot C_d)})$. The parametric sweep (Section 3.2) validates $f_0 \propto \sqrt{g}$: sweeping g from 0.3 to 0.7 mm shifts the resonance from 9.2 to 10.8 GHz. At optimal $g = 0.5$ mm, the SRR resonance targets the 10 GHz coupling peak, yielding ∼8 dB isolation improvement and reducing ECC from ∼0.05 to 0.018. Isolation remains better than −19 dB for ±0.1 mm variations, confirming manufacturing robustness.

5. ANTENNA FIELD MEASUREMENT AND RESULTS

To further verify the performance of the antenna, a prototype was manufactured. Figure 15 shows the fabricated prototype of the proposed antenna. Figure 16 shows the comparison of the S-parameter simulation and measurement results for the UWB-MIMO antenna. It can be seen from the figure that the simulated and measured S-parameters are basically consistent. Within the measured frequency band, S_{11} is less than −10 dB, and S_{21} is less than −18 dB. The simulation results indicate that the parameters of the MIMO-UWB notch antenna meet the requirements for MIMO-UWB systems in practical engineering applications.

Figure 17 compares the simulated and measured radiation patterns of the proposed ultra-wideband antenna over the 3–9 GHz band, showing strong agreement in both main lobe direction and overall shape across the frequency range. This consistency confirms stable radiation performance throughout the operating band and validates the accuracy of the simulation model, as well as the reliability of the antenna design.

6. CONCLUSION

In conclusion, this study presents a compact metamaterial-integrated UWB-MIMO antenna with multi-notch functionality. The design features a novel synergistic decoupling mechanism consisting of bent stubs for low-frequency coupling sup-

pression and an embedded split-ring resonator (SRR) metamaterial unit, which provides superior high-frequency decoupling performance. This structural configuration enables a measured isolation (S_{21}) better than -21 dB across the entire 3.1–13 GHz UWB spectrum.

Complemented by an optimized radiating patch and a strategic slot-loading design, the antenna achieves full ultra-wideband coverage while realizing four precisely controlled notch bands targeting interference from WiMAX (3.3–3.4 GHz), WLAN (5.15–5.825 GHz), 5G n79 (4.4–5.0 GHz), and satellite uplink (7.9–8.4 GHz) systems. The antenna's outstanding performance is validated through measurements, demonstrating stable omnidirectional radiation patterns, an ultra-low envelope correlation coefficient (ECC $<$ 0.018), and near-ideal diversity gain (DG $\approx$ 10 dBi) throughout the operating band — all accomplished within a compact footprint of 60×32 mm.

By successfully integrating innovative metamaterial decoupling techniques with multi-band interference rejection capabilities, the proposed antenna achieves an exceptional balance between miniaturization, isolation performance, and spectral selectivity. This makes it a highly competitive solution for advanced UWB-MIMO communication systems, with strong potential for practical applications in modern wireless environments.

ACKNOWLEDGEMENT

This paper was funded by the National Natural Science Foundation of China (61803356). This paper was supported by the Jilin Provincial Department of Education Science Research Project, with the project number JJKH20261429KJ.

REFERENCES

[1] Zheng, X., Z. Zhao, Y. Zhang, T. Zhang, A. Gui, and H. Wu, "A low-coupling broadband MIMO array antenna design for Ku-band based on metamaterials," *Journal of Electromagnetic Engineering and Science*, Vol. 24, No. 6, 666–673, 2024.

[2] Zheng, X., L. Yue, and Y. Zhang, "A compact four-port axially symmetric UWB-MIMO antenna array: Metamaterial-integrated coplanar waveguide for broadband operation with high isolation," *Progress In Electromagnetics Research C*, Vol. 162, 58–69, 2025.

[3] Jusoh, M., M. F. Bin Jamlos, M. R. Kamarudin, and M. F. Bin Abd Malek, "A MIMO antenna design challenges for UWB application," *Progress In Electromagnetics Research B*, Vol. 36, 357–371, 2012.

[4] Su, J., Y. Li, X. Chen, G. Han, and W. Zhang, "A compact triple band-notched quasi-self-complementary UWB MIMO antenna decoupled by SRRs," *International Journal of Microwave and Wireless Technologies*, Vol. 15, No. 7, 1251–1261, Sep. 2023.

[5] Gao, M., J. Wang, J. Nan, and X. Han, "Design of a compact triple-notch UWB-MIMO antenna," *Journal of Electronic Measurement and Instrumentation*, Vol. 36, No. 6, 144–151, 2022.

[6] Mishra, N. K., J. Acharjee, V. Sharma, C. Tamrakar, and L. Dewangan, "Mutual coupling reduction between the cylindrical dielectric resonator antenna using split ring resonator based structure," *AEU Int. J. Electron. Commun.*, Vol. 154, 154305, Sep. 2022.

[7] Zheng, X. and X. Xu, "Design of planar ultra-wideband notch antenna," in *2021 19th International Conference on Optical Communications and Networks (ICOCN)*, 1–3, Qufu, China, 2021.

[8] Li, J.-F., Q.-X. Chu, Z.-H. Li, and X.-X. Xia, "Compact dual band-notched UWB MIMO antenna with high isolation," *IEEE Transactions on Antennas and Propagation*, Vol. 61, No. 9, 4759–4766, Sept. 2023.

[9] Wu, A., M. Zhao, P. Zhang, and Z. Zhang, "A compact four-port MIMO antenna for UWB applications," *Sensors*, Vol. 22, No. 15, 5788, 2022.

[10] Saad, A. A. R. and H. A. Mohamed, "Conceptual design of a compact four-element UWB MIMO slot antenna array," *IET Microwaves, Antennas & Propagation*, Vol. 13, No. 2, 208–215, 2019.

[11] Yang, L., M. Xu, and C. Li, "Four-element MIMO antenna system for UWB applications," *Radioengineering*, Vol. 28, No. 1, 60–67, 2019.

[12] Kumar, S., G. H. Lee, D. H. Kim, W. Mohyuddin, H. C. Choi, and K. W. Kim, "A compact four-port UWB MIMO antenna with connected ground and wide axial ratio bandwidth," *International Journal of Microwave and Wireless Technologies*, Vol. 12, No. 1, 75–85, 2020.

[13] Jairath, K., N. Singh, V. Jagota, and M. Shabaz, "Compact ultrawide band metamaterial-inspired split ring resonator structure loaded band notched antenna," *Mathematical Problems in Engineering*, Vol. 2021, No. 1, 5174455, 2021.

[14] Tang, Z., X. Wu, J. Zhan, S. Hu, Z. Xi, and Y. Liu, "Compact UWB-MIMO antenna with high isolation and triple band-notched characteristics," *IEEE Access*, Vol. 7, 19 856–19 865, 2019.

[15] Saraswat, R. K. and M. Kumar, "A metamaterial hepta-band antenna for wireless applications with specific absorption rate reduction," *International Journal of RF and Microwave Computer-Aided Engineering*, Vol. 29, No. 10, e21824, 2019.

[16] Saraswat, R. K. and M. Kumar, "A vertex-fed hexa-band frequency reconfigurable antenna for wireless applications," *International Journal of RF and Microwave Computer-Aided Engineering*, Vol. 29, No. 10, e21893, 2019.

[17] Saraswat, R. K. and M. Kumar, "Implementation of metamaterial loading to miniaturized UWB dipole antenna for WLAN and WiMAX applications with tunability characteristics," *IETE Journal of Research*, Vol. 68, No. 3, 2022–2035, 2022.